

Observation of Sediment Mobilization by an Internal Solibore on the California Inner Shelf

J. Jefferson¹, J. Simeonov², J. Calantoni², and A. Sheremet¹

¹Engineering School of Sustainable Infrastructure and Environment, University of Florida, Gainesville, FL, USA,

²Ocean Sciences Division, U.S. Naval Research Laboratory, Stennis MS, USA

Key Points:

- Observations of sediment transport generated by a cross shore propagating internal solibore are reported and discussed
- Near bed velocities generated by the internal tidal bore create bed shear stresses large enough to mobilize sediment
- The results of the study are relevant to inner continental shelf environments that experience intense internal wave activity

Corresponding author: J. Jefferson, josephjefferson@ufl.edu

Abstract

Acoustic backscatter, velocimetry measurements of the nearbed velocity profiles, and thermometer chain measurements of the temperature stratification were used to understand the bottom boundary layer flows and associated sediment transport processes in 35 meters water depth on the California shelf off of Point Sal where the bottom sediment consists of fine sand with median grain size diameter of $d_{50} = 0.1$ mm. The observations show that the nearbed flow is dominated by the bore of a shoaling internal tide whose steepening front generated a series of internal solitary waves (ISW) with a 15-min period superposed on the tail of the bore. The bore-induced nearbed flow was strongly asymmetric with 20 cm/s seaward directed flow under the bore trough that exceeded the bottom stress threshold for mobilization of the 0.1 mm sand, and 5-10 cm/s onshore flow during the tail of the bore that produced only subcritical bottom stress. The ISWs induced symmetric 5-10 cm/s nearbed velocity which however combined with the bore tail to produce onshore flows under the wave crests with bottom stress that also exceeded the sediment mobilization threshold.

Plain Language Summary

Indirect investigation of the bottom boundary layer behavior under internal wave forcing was conducted in 35 m of water off the central California coast. High resolution observations of the internal waves, near bed velocity profiles, and sediment transport were obtained from chains of temperature sensors and near bed acoustic instrumentation. Time series records collected on September 15, 2017 shows the presence of an internal tidal bore which has likely begun the process of shoaling, where the bore front proceeds a train of internal solitary waves. The strongest flows were observed during the arrival of the bore front creating near bed shear stresses large enough to mobilize fine grained sandy sediments with a median grain size of 0.1 mm. The flow direction associated with the internal tidal bore is directed in the offshore direction suggesting sediments are initially transported off shore. The individual internal solitary waves also work to further mobilize and transport sediments with the largest shear stresses observed to coincide with the peak flow of the internal solitary waves. The peak flow associated with the internal solitary waves is directed in the onshore direction suggesting that the internal solitary waves transport sediments on shore.

1 Introduction

Internal waves research is a mature research field. No list of references can do justice to its breadth and diversity, but synoptic views on the topic may be found in many review papers (e.g., Levine (1983); Helfrich and Melville (2006); Whalen et al. (2020) and many others) and substantive monographs (e.g., Miropol'sky (2001); Sutherland (2014); Vallis (2017) and many others). The question of the role of internal waves in transporting sediment over the shelf has been asked early on. Field observations and numerical studies (e.g., Karl et al., 1986; Boczar-Karakiewicz et al., 1991; Cacchione & Drake, 1986; Bogucki et al., 1997; Bogucki & Redekopp, 1999; Noble & Xu, 2003), see also the review by (Boegman & Stastna, 2019) suggested that internal wave flows may be strong enough to generate significant sediment transport and thus play an important role in the dynamics of large scale bedforms on the shelf. While a large fraction of the sediment transported across the shelf is typically detected as bedload mobilized by increased nearbed shear stresses under internal wave flows (e.g., Nittrouer & Wright, 1994; Quaresma et al., 2007), significant quantities of sediment have been observed above the boundary layer, attributed to a global instability mechanisms, i.e., driven by the global properties of the flow, as opposed to the local flow profile (e.g., Bogucki et al., 1997; Bogucki & Redekopp, 1999; Stastna & Lamb, 2002; Diamessis & Redekopp, 2006; Aghsaee et al., 2012). Although further studies reproduced the mechanism in the laboratory (e.g., Carr et al., 2008; Agh-

sae & Boegman, 2015), its importance in the field has yet to be confirmed. An analysis conducted by Zulberti et al. (2020) of high resolution observations of internal waves collected near the 250-m isobath on the Australian shelf (Rayson et al., 2019) failed to find strong evidence of the global instability mechanisms. Instead, they conclude that at the experiment site sediment transport is driven by a combination of bed shear stress intensification, turbulent transport, and a vertical pumping mechanism associated with the compression and expansion of the bottom boundary layer.

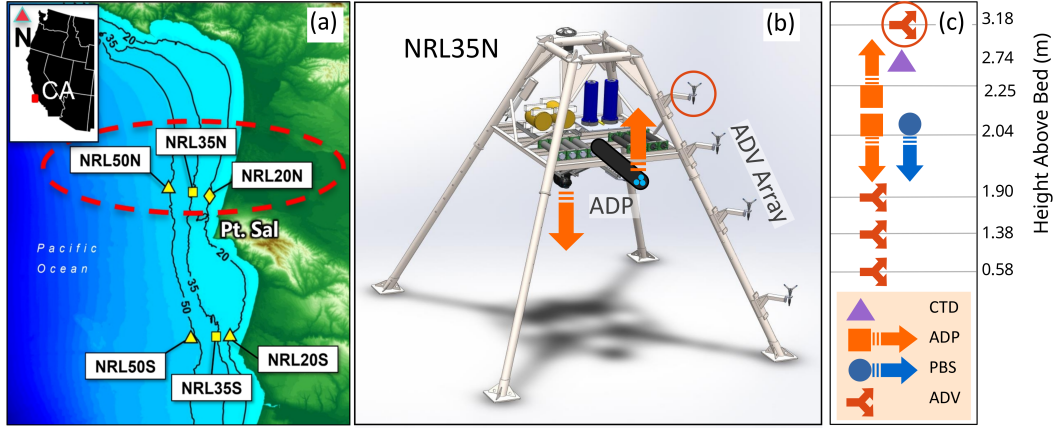
However, the question of what role different instability mechanisms play in sediment resuspension under internal waves cannot be considered settled, because it is not clear to what degree the results of Zulberti et al. (2020) are specific for the site investigated. Boegman and Stastna (2019) argue that our understanding of sediment transport mechanisms has been severely limited by the quality and quantity of field observations available. While field observations have been steadily improving in resolution and in the physical aspects covered, they remain prohibitively expensive. The comprehensive Inner Shelf Dynamics Experiment (2017), a collaborative effort involving 14 universities and research institutions, organized by the Naval Research Laboratory and the Office of Naval Research (e.g., McSweeney et al., 2019; Kumar et al., 2021), provides an excellent opportunity to investigate sediment resuspension mechanisms, this time on the USA West Coast shelf. The experiment monitored shelf processes near Point Sal, CA, covering over 50 km along the coast, from 50-m depth to the shoreline. The richness of the data collected using a diversity of instruments, ranging from marine radar, SAR, and ship surveys to high resolution mooring including thermistor chains, quadpods monitoring nearbed turbulence, pencil beam sonars, etc, is unprecedented.

The analysis presented here analyzes observations collected by the moorings deployed by Naval Research Laboratory near the 50-m, 35-m and 20-m isobaths, with a focus on the 35-m mooring, which was equipped with high resolution instrumentation for monitoring the flow in the first 3 m above the bed. In this region, the analysis of McSweeney et al. (2019) shows that flow was dominated by nonlinear shoaling and breaking of internal tidal bores of approximately 6-hr period propagating toward the shore. Through weakly nonlinear shoaling, the tidal bores often develop dispersive (undular) patterns, that can generate strong nearbed currents and potentially mobilize and resuspend sediments. Section (2) provides a brief overview of the field experiment, the types of data used and data analysis methods, and sediment transport theory. The results of the analysis are presented in section (3). In section (4) we discuss the results in the context of previous studies and suggest possible directions for future research.

2 Methods

2.1 Field Experiment

The observations analyzed in this study were collected by the Navy Research Laboratory (NRL) during the Inner Shelf field experiment (Kumar et al., 2021), in September 2017. The NRL experiment deployed moorings near the 50-m, 35-m and 20-m isobaths along two roughly east-west transects (figure 1a). Here, we analyze the data collected by the NRL 35-m isobath mooring (NRL35N in figure 1a). The location and configuration of the instruments is shown in 1b-c. The temperature stratification was monitored by thermistor chains which deployed 10 temperature sensors spaced at approximately 3 m vertically. Three-dimensional velocity profiles were measured by two acoustic Doppler profilers (ADP, Nortek Aquadopp), one looking up and one down, together covering of about 3 m in the boundary layer with a vertical resolution of 5 cm. Four acoustic Doppler velocimeters (ADV, Nortek Vector) provided independent, point measurements. All Doppler instruments also recorded acoustic backscatter information, used here as a proxy for suspended sediment concentration. Salinity was monitored using a Sea-Bird CTD Profiler. All times reported here are Local Standard Time.



Instrument	Type	Variable	Elevation (mab)	Sampling\Burst (Hz\min)	Resolution (m)
Sea-Bird Sci. SBE 56	Thermistor	T	3	1\-	3(v)
Nortek Aquadopp	ADP	PUVWB	2.04	2\30	0.05(v)
Nortek Vector	ADV	PUVWB	3.18	32\30	-
Imagenex 881A	Sonar	Hab	2.05	-\60	0.002(v), 0.025(h)
Sea-Bird Sci. CTD	Salinity	ST	2.74	1\-	-

Figure 1. Field experiment and instrumentation used in this study. (a) NRL sites during the Inner Shelf Dynamics Experiment near Point Sal, CA. Inset: California coast. Each mooring included a thermistor chain (not shown) and bottom mounted hydrodynamic instrumentation. (b) A schematic of the NRL35N instrumented bottom quadpod. (c) Position above the bed of instruments used in this study. Arrows indicate the direction of the profiling beam. The ADV used in this study is marked by a red circle. The up-looking ADP was not used, due to frame interference. Details of the configuration of the instruments used in this study are given in the table. Acronyms: ADV – acoustic Doppler velocimeter; ADP – acoustic Doppler profiler; CTD – conductivity, temperature, depth. Variables: P – pressure; UVW – velocity vector, either profile or single point measurement, in the east/north/up directions; B – acoustic backscatter; S – salinity; T – temperature; Hab – height above bed. Instrument resolution is marked by (v) – vertical, and (h) – along beam. The elevation of the instruments is given in mab (meters above bed).

2.2 Hydrodynamics and stratification

The temperature stratification profiles provided by the thermistor chain were smoothed and interpolated vertically to a resolution of 20 cm using a cubic smoothing spline (Matlab[®] function `csaps`), and converted to density using the standard equation of state (e.g., Mas- sel, 2015) for a mean salinity of 33 ‰, obtained from CTD readings. The position of the pycnocline was estimated here using the density-weighted mean

$$h_P = \int_0^H z \frac{\partial \rho}{\partial z} dz. \quad (1)$$

The frequency content of the pycnocline time series between Sep. 14th and 16th, 2017, was estimated using a windowed Fourier transform with a sliding window of ≈ 4.3 hr with 90% overlap. The windowed Fourier transform $G_\tau(f)$ of a real function of time $g(t)$, is

defined as

$$G_\tau(f) = \int g(t)\psi_{f,\tau}^*(t)dt, \quad g(t) = \int \int_{-\infty}^{\infty} G_\tau(f)\psi_{f,\tau}(t)df d\tau, \quad (2)$$

where the asterisk denotes complex conjugation, $\psi_{f,\tau}$ is a set of elementary functions such that

$$\psi_{f,\tau}(t) = w_\tau(t)e^{2\pi ift}, \quad \int_{-\infty}^{\infty} w(t-\tau)dt = 1, \quad (3)$$

and the window $w(t)$ is a real function of half-length a , i.e., $w(t) = 0$ for $|t| \geq a$. The spectrogram of g , defined as $\log_{10} |G_\tau(f)|^2$, provides a measure of the instantaneous power distribution over frequencies f . The inverse windowed Fourier transform was computed using the Matlab[®] algorithm by Zhivomirov (2019).

The power spectrum of the stationary oscillations with period ≥ 1 hr was estimated using the Welch method (Welch, 1967). The 10-day time series was divided into 34-hr segments with 50% overlap, and tapered using a Hann window, resulting in a spectral estimate with 14 degrees of freedom.

To reconstruct the flow in the boundary layer, the velocity time series collected by the ADPs and the highest 3.18-mab ADV (red circle, figure 1) were despiked (Goring & Nikora, 2002), and further corrected by removing velocity values corresponding to low (<70) beam correlations. Velocity measurements collected by the up-looking ADP showed significant interference from the quadpod frame. Down-looking ADP records also show frame interference above ≈ 1.5 mab (meters above bed), and corrupt measurements in the 4 vertical bins closest to the bed. In the analysis below, we use the measurements collected by the down-looking ADP, covering elevations from 0.18 to 1.8 mab (ADP blanking distance ≈ 0.10 m) and the top ADV, located at 3.18 mab. Running averages with sliding windows of 15 min and 4 min were used to identify internal bores and tides, respectively.

2.3 Sediment transport

Following previous work (Quaresma et al., 2007; Richards et al., 2013; Zulberti et al., 2020), we use the backscatter intensity as measure of the suspended sediment concentration. To eliminate instrument beam-forming bias, the backscatter intensity measurements were de-meant at each vertical bin, smoothed using a 4-min running average, and normalized to the interval of 0-1. The backscatter magnitude reported here is the average over all three beams of the instrument. The backscatter intensity reported by acoustic instruments has a rather complicated dependency on the size and amount of particles suspended (e.g., Sheng & Hay, 1988; Thorne et al., 1993; Thorne & Hanes, 2002; Sahin et al., 2012). Due to the lack of independent measurements needed for a quantitative calibration (Sahin et al., 2012; Meral, 2016; ?, ?) a quantitative estimation of suspended sediment concentration was not further pursued.

2.4 Sediment transport models

We assume that, main driver of sediment mobilization and resuspension at time scales characteristic for internal waves is the bottom shear stress, estimated here using two independent formulations, the logarithmic velocity profile model, and the wave-current bottom friction empirical model (Grant & Madsen, 1979; Ribberink, 1998). In the logarithmic velocity profile model, the bottom shear stress may be written as

$$\tau^{\log} = \rho u_*^2, \quad \text{with } U(z) = \frac{u_*}{k} \ln \left(\frac{z}{z_0} \right) \quad (4)$$

where z is the height above the bed, z_0 is the roughness length, U is the mean velocity profile, u_* is the friction velocity, and $k = 0.41$ is the von Karman constant. The u_*

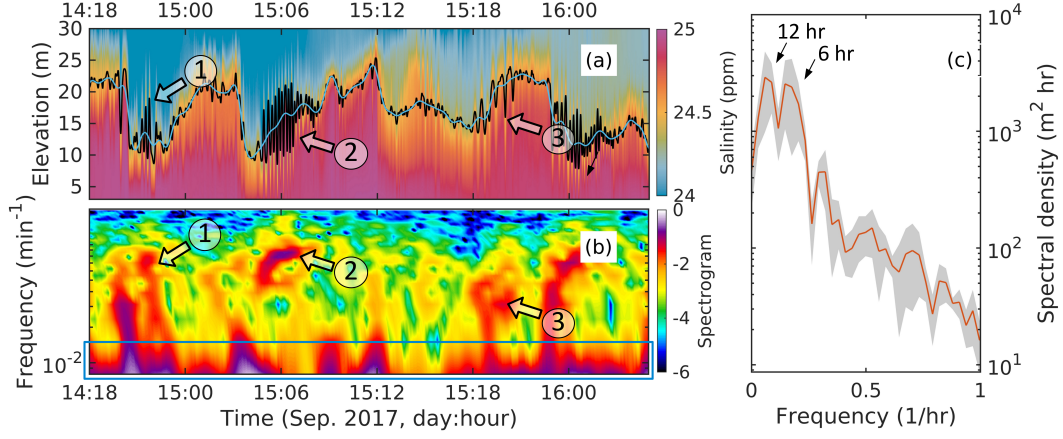


Figure 2. Stratification analysis. a) Pycnocline elevation estimate (black line; equation 1) and bore component (blue) at the 35-m NRL site for Sept. 14-16th 2017. b) Normalized spectrogram of the pycnocline (black line in panel a). The bore component of the pycnocline (blue line in panel a) was reconstructed by inverting the windowed Fourier transform in the low frequency band, marked by a blue rectangle. Arrows mark internal wave packets. c) Spectral density of the bore component of the pycnocline. The grayed area has a vertical span equal to the standard deviation of the spectral estimate.

and z_0 , the velocity time series provided by the upward looking ADP were filtered using a 4-min running average. A linear regression fit was applied progressively to the ADP profile, starting from a minimum of 3 lowest valid velocity profile points, and iteratively including higher elevation measurement bins until the relative error exceeds some arbitrary tolerance. The linear profiles estimates retained have positive slopes.

Alternatively, following Ribberink (1998, equations 9-10), the shear stress may be estimated as

$$\tau^{\text{fr}} = \frac{1}{2} \rho f u \mathbf{u}, \text{ with } f = 2 \left(\frac{\kappa}{\ln(\delta/z_0)} \right)^2 \quad (5)$$

where \mathbf{u} is the velocity vector of magnitude u at an arbitrary level $z = \delta$ above the bed in the logarithmic layer, κ is the von Karman constant, and $z_0 = k_s/30$ is the roughness length, with k_s the characteristic Nikuradse grain roughness, $k_s \approx 3d_{90}$. Ribberink (1998) notes that this “near-bed” approximation is also applicable to non-uniform and non-steady flows.

The efficiency of the bottom stress to mobilize sediments is usually quantified by the nondimensional Shields parameter (van Rijn, 1984)

$$\theta = \frac{\tau}{(\rho_s - \rho) g d_{50}}. \quad (6)$$

where ρ_s is the sediment density, $\rho = 1026 \text{ kg/m}^3$ is the density of saline water, g is the gravitational acceleration. Empirical data has shown that sediment can be mobilized only when the Shields parameter exceeds a critical value θ_c that depends on the sediment grain size. A commonly used empirical estimate of the threshold Shields parameter is given by (??, ?)

$$\theta = \frac{0.3}{1 + 1.2 D_*} + 0.055 (1 - e^{-0.02 D_*}), \text{ where } D_* = d_{50} \left(\frac{g(\rho_s - \rho)}{\rho \nu^2} \right)^{1/3}, \quad (7)$$

where $\nu = 1.19 \times 10^{-6} \text{ m}^2/\text{s}$ is the kinematic viscosity of water and $s = \rho_s/\rho$. Sediment grab samples indicate that 91% of the sediment was sand particles with a median

grain size of $d_{50} = 0.1$ mm. With these values, the Shields number is $\theta \approx 0.084$. However, the empirical threshold of motion data (e.g., Nielsen, 1992, Fig. 2.2.2) exhibits significant scatter such that the threshold of motion Shields value for $d_{50} = 0.1$ mm spans the range $[0.055, 0.084]$. The corresponding range of the dimensional critical bottom shear stress (equation 6) is $0.088 \text{ Nm}^2 < \tau_c < 0.135 \text{ Nm}^2$. The friction velocity is also used to quantify a threshold for the bottom turbulence that is needed to move the bed particles into suspension. The threshold value of the friction velocity is approximately equal to particle fall velocity scale

$$w_s = [(s - 1)gd_{50}]^{1/2} \quad (8)$$

For the sediment grain size at our experimental site the threshold friction velocity for suspension is $u_* = w_s = 4.1 \text{ cm/s}$.

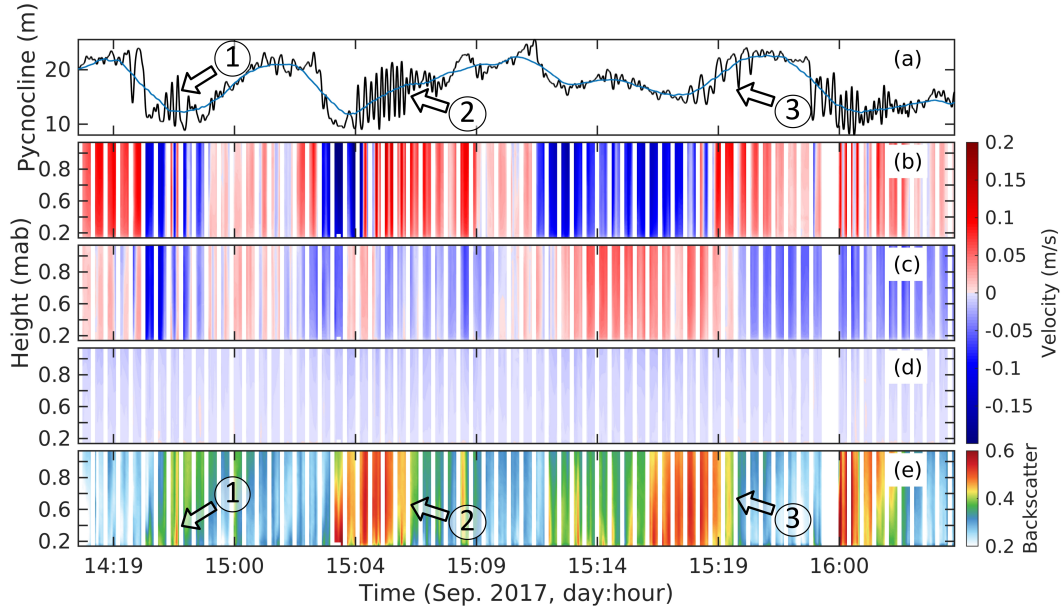


Figure 3. Flow and acoustic backscatter recorded at the 35-m NRL site by the down-looking Aquadopp between Sept. 14th and 16th 2017. a) Pycnocline (black line in figure 2a). Velocity profile (figure 1b-c): east (b.), north (c.), and vertical (d.) velocity components (positive directions are east, north and up). d) Acoustic backscatter profile (arbitrary units). All time series are smoothed using a 4-min running average.

3 Results

3.1 Vertical structure of the flow in the boundary layer.

At the 35-m mooring, the pycnocline frequency content shows bursts of transient oscillations (internal waves) with periods between 15 min and 30 min superposed on low frequency oscillations dominated by a semi- and quarter-diurnal bores (figure 2). The bores are generated as depression waves by the interaction of the barotropic tide with topography (McSweeney et al., 2019), and undergo a weak nonlinear shoaling evolution as they propagate into shallower water. In contrast with the near-stationary bore oscillations, the internal wave population intermittent and is more diverse. Within approximately a day (Sep. 15th, 2017, figure 2), the shape of the pycnocline exhibits structures that could be described as a packet of solitary waves of elevation, event (1); an undular bore (solibore) of depression, event (2), mean period ≈ 15 min; and solitary waves of

depression, event (3). In agreement with the analysis of McSweeney et al. (2019), the flow generated by the combined bore and internal waves is mainly oriented along the east-west direction, with maximum nearbed velocities in the order of 0.2 m/s, with much weaker north and vertical components (figure 3b-d). The backscatter intensity recorded by the velocity profiler (figure 3e), shows bursts of intensity that correlate the occurrence of internal wave, suggesting sediment mobilization and transport.

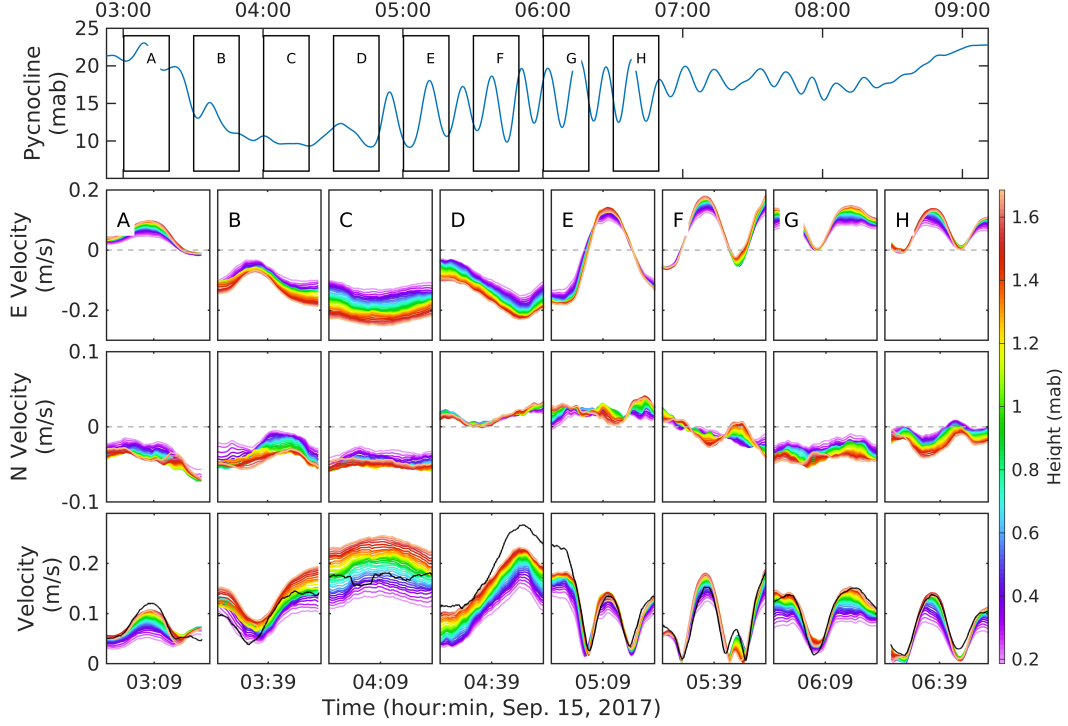


Figure 4. Flow velocity associated with the solibore event (2) in figure 2. Top to bottom: smoothed pycnocline (blue line, figure 2a); east velocity component; north velocity component; horizontal velocity magnitude. The color coded velocity profiles measured by the down-looking Aquadopp (figure 1b-c) are smoothed with a 4-min running average. The black lines are ADV measurements. Measurement bursts are marked by letters *A* to *H*, and by black rectangles in the top panel.

This study focuses the solibore event (2) in figure (2). Figure (4) show details of the solibore, including the pycnocline oscillations and the vertical structure of nearbed velocity. At the bore trough (minimum elevation, bursts *C* and *D*), the flow velocity reached maximum magnitude ≈ 0.25 m/s westward (≈ -168 deg counterclockwise from east). The east-west flow direction was maintained at the back of the bore, where the wave packet dominated the flow, with total velocity slightly less than 0.2 m/s at wave crests (maximum pycnocline elevation). In general, the velocity measured by the ADV located at 3.18 mab (red circle in figure (1)c upper-bound elevation of the quadpod array) is comparable with, or larger than the maximum velocity recorded by the down-looking Aquadopp (top measurement bin at 1.3 mab), which suggests that the boundary layer was contained within the range of the array, and that the top ADV measurements may be identified with the free stream velocity. This is not true for bursts *B* and *C*, which show larger velocities near the bottom. The anomaly might be caused by interference from the quadpod frame: although measurements elevations showing obvious frame interference were

229 excluded, in bursts *B* and *C*, the the larger velocities might have caused interference at
 230 lower elevations.

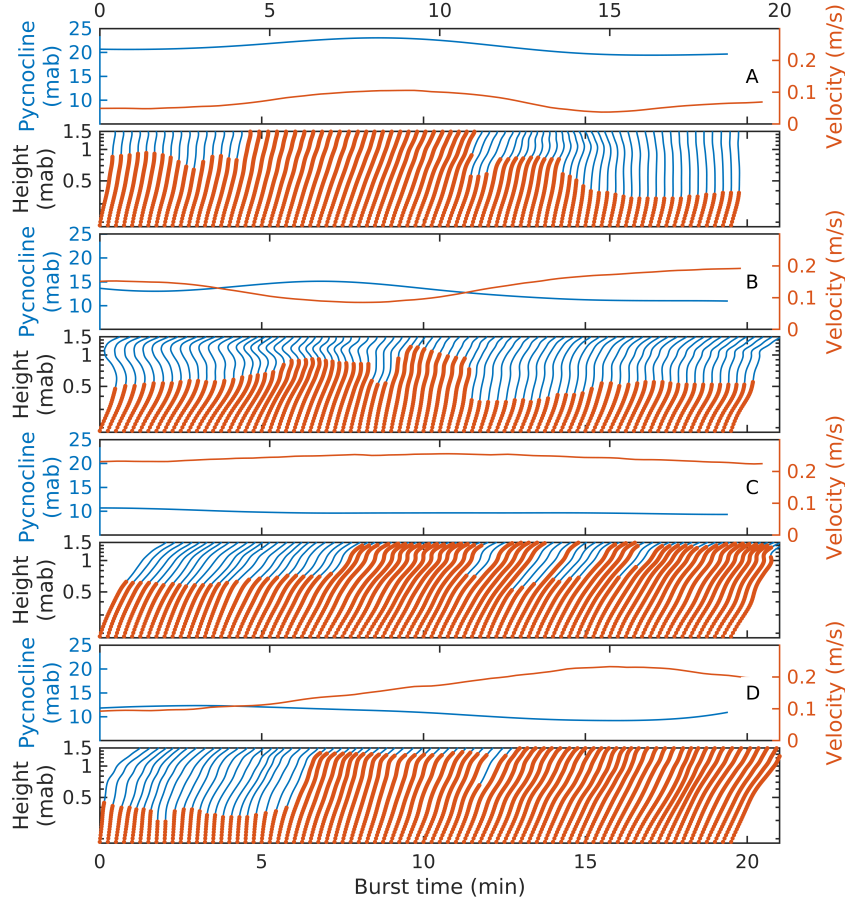


Figure 5. Vertical structure of the horizontal velocity magnitude for each of the measurement bursts marked in figure (4). The extent of the linear regression fit (with a relative tolerance of 10^2 and $R^2 > 0.98$) is marked with red dots.

231 The log boundary layer model (equation 4) produces consistent estimates for u_* ,
 232 z_0 , and the log layer thickness for values of the coefficient of determination $R^2 > R_{tol}^2$
 233 (figures 5-7 show estimates for $R_{tol}^2 = 0.98$; compare with figure (4)). The parameters
 234 are strongly correlated to the bore/internal wave phases. During the time period dom-
 235 inated by the bore, measurement bursts *A* to *D*, covering the front and trough of the in-
 236 ternal bore, the parameters vary slowly, with the log layer thickness between 0.30 and
 237 1.5 mab and the friction velocity (figure 5) fluctuating between 1 and 2 cm/s (figure 7). Despite
 238 high R^2 values, the log layer thickness exhibits some discontinuities, e.g., between min-
 239 utes 10 and 15 of measurement burst *C*, that seem to be caused by localized random de-
 240 viations from a log profile.

241 Under the internal wave packet, bursts *E-H*, (figures 6-7), the log model results are
 242 strongly correlated with the internal wave phase. In general, both the log-layer thick-
 243 ness and the friction velocity grow under wave crests and decrease under wave troughs.
 244 The log model fails when the flow velocity magnitude approaches zero, e.g., minutes 6-
 245 7 of burst *E*; minutes 4, 12, and 15, burst *F*; minutes 3 and 14, burst *H* (figure 6). These
 246 flow reversals do not coincide with the inflection point of the pycnocline oscillations be-

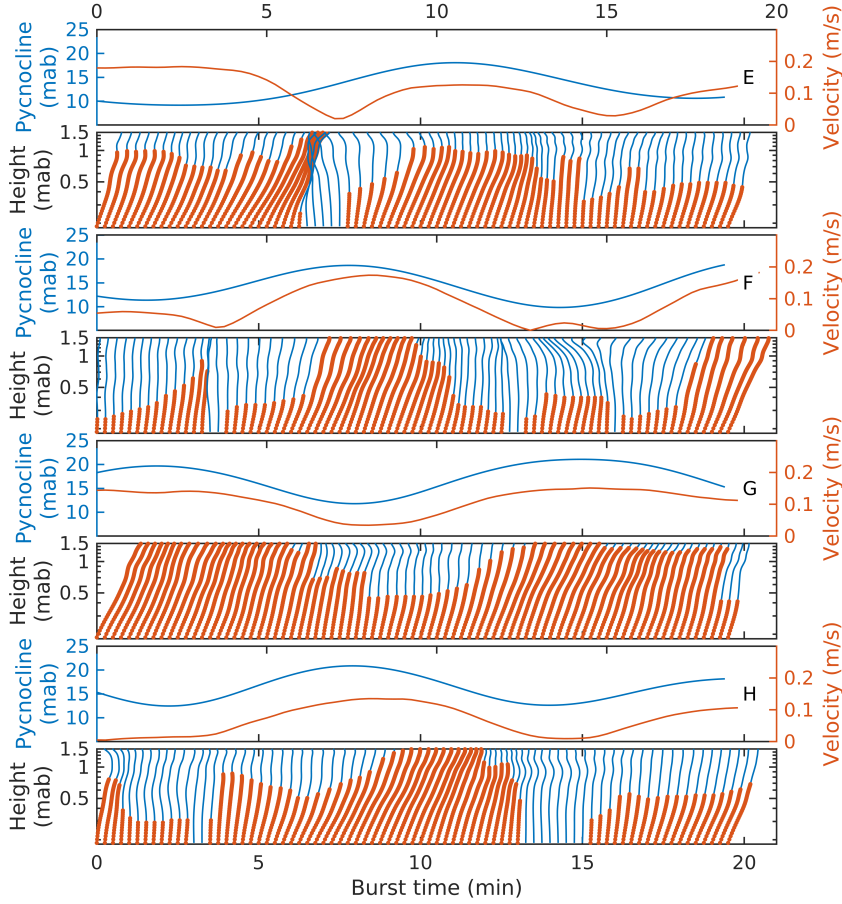


Figure 6. Same as figure 5, for the remaining measurements bursts considered here. Linear profile estimates corresponding to friction velocity values less than 10^{-3} are not included in the plot.

cause the internal wave oscillations are modulated by the bore phase. The internal wave oscillations are, however, modulated by the bore phase: in burst *G*, the background bore flow maintains non-zero velocity and the log layer thickness is continuous.

While the bottom stress estimate τ^{log} (equation 4) is as robust as the u_* estimate, the friction estimate τ^{fr} (estimate 5) is more tenuous because we lack a good estimate of the roughness length, and because there are times when the top of the log/boundary layer appears to exceed the top of the ADP measurement range. Figure (8), middle panel, shows the evolution of τ^{lg} and estimates of τ^{fr} using the time average roughness length $z_0 = 1$ cm and, for the reference height δ and $\mathbf{u}(\delta)$, either the log layer thickness and the velocity at the top of the log layer, or the ADV velocity measurement and its respective height of 3.15 mab (figures 5-6). The different estimates agree well over burst *D* and for the duration of the internal wave packet (bursts *E* to *H*), but there is significant disagreement during the through of the bore in bursts *B* and *C*. This is consistent with the observation that the ADV velocity generally follows the ADP velocity (figure 4) except in bursts *B* and *C* when the ADV velocity is significantly smaller than that at the top of the ADP range.

3.2 Sediment transport

In the absence of direct measurements of suspended sediment concentration, we compare the stresses to the profile of the acoustic backscatter recorded by the down-looking ADP (see figure 8, lower panel for a qualitative discussion of sediment transport processes). Although ADP backscatter intensity is typically biased high for measurement bins located at large distance from transducer, due to scattering and absorption by a thicker layer of fluid (e.g., (Sahin et al., 2012), figures 4-5), in this case the ADP was looking down toward the bed, where concentrations are naturally higher. Backscatter measurements suggest that suspended sediment presence is negligible during bursts *A* and *B*, but becomes significant in the entire ensonified water column during bursts *C* to *H*. This largely agrees with the bottom stress estimates: during *A* the stress is too low to suggest mobilization; during bursts *C*, and *E* to *H*, the stress maxima close to τ_c match remarkably well with periods of large backscatter. We should note, however, that the observed backscatter is likely due to sediments finer than d_{50} because the friction velocity u_* (figure 7) never exceeds the threshold value $w_s = 4.1$ cm/s for suspension of $d_{50} = 0.1$ mm.

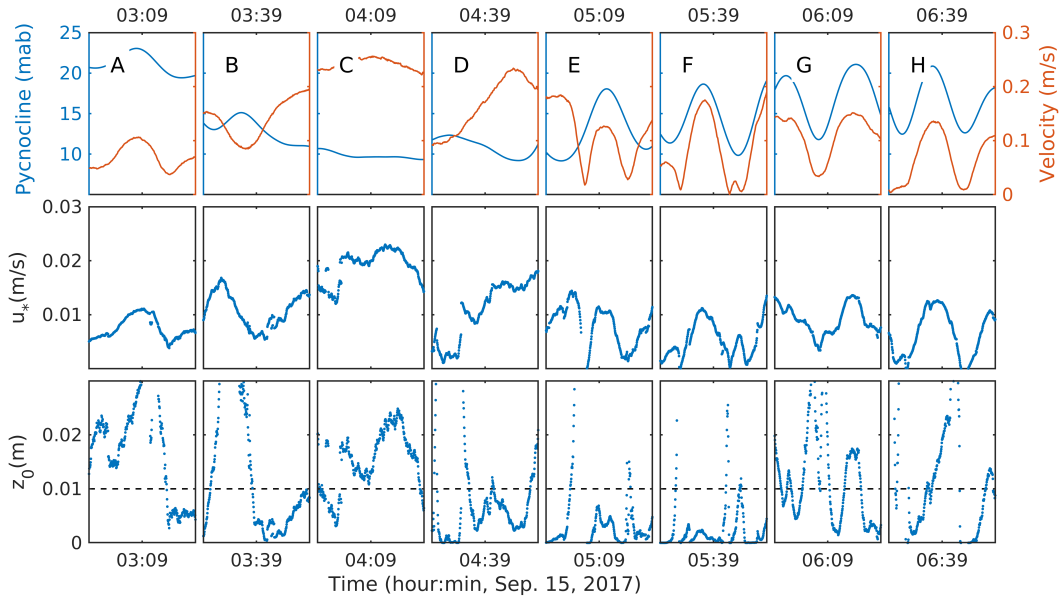


Figure 7. Estimates of the parameters of the log layer model (4) for all measurement bursts considered in this study. Top row: Pycnocline elevation and magnitude of flow velocity at 1.68 mab (topmost valid measurement bin of the down-looking ADP). Middle row: friction velocity u_* . Bottom row: the intercept value z_0 .

Next, we will use the estimated bottom stresses to discuss the likely nature and direction of sediment transport. Assuming that the acoustic backscatter is a proxy for suspended sediment concentration, its evolution under the bore structure indicates the direction of sediment transport. At the NRL35N location, the tidal bore is an asymmetric wave of depression, with a steep front and mild back (figure 4, top panel), and flow velocity negatively skewed, with large trough flow velocity oriented westward (seaward) (figure 4, burst *C*). At the trough, the flow creates bottom stresses that exceed the mobilization threshold for $d_{50} = 0.1$ mm by a factor of five (figure 8), and is expected to generate bedload transport in the current ripples regime (e.g., (Allen, 1982), Figure 8-23). The flow direction under the bore suggests that this bedload transport is directed seaward. During the peak trough flow in burst *C*, the Shields parameter ranged in $0.13 < \theta < 0.29$ and the range of the hydraulic friction factor $0.1 < f = 2u_*/u(\delta) <$

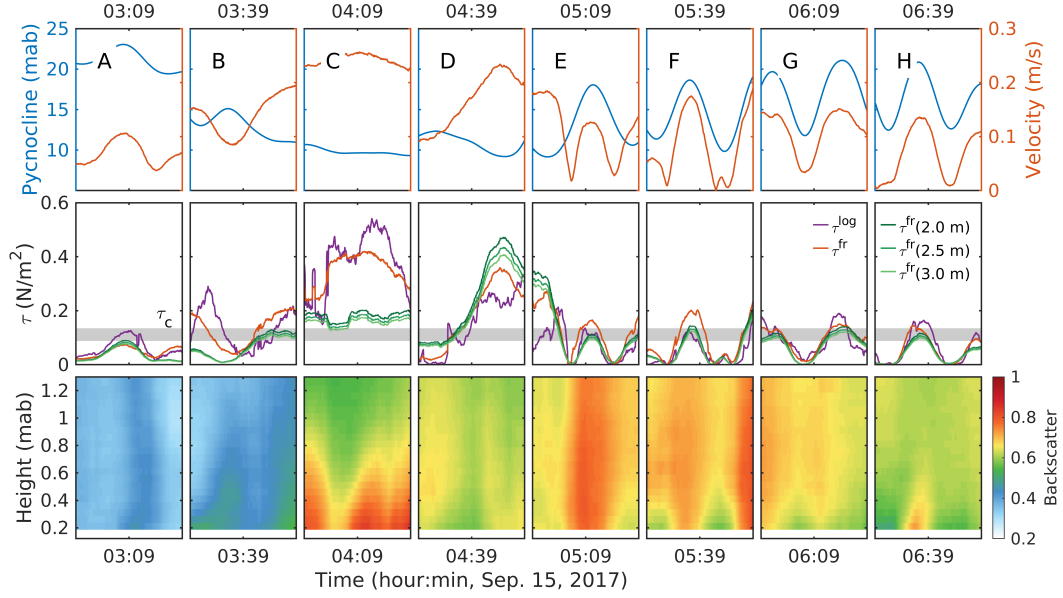


Figure 8. Evolution of essential sediment transport parameters for all measurement bursts considered in this study (compare with figures 7). Top row: Pycnocline elevation and magnitude of flow velocity at 1.68 mab (topmost valid measurement bin of the down-looking ADP). Middle row: Estimates of bottom stress – τ^{\log} (purple) provided by the log layer model, equation (4); and τ^{fr} given by the friction model, equation (5) using different values for the reference velocity $u(z = \delta)$: $u(\delta)$ at the top $z = \delta$ of the log layer (red); and assuming that the ADV measurements (3.18 mab) represent the free stream velocity, and using as $\delta = 2, 2.5$ and 3 mab as approximations for the boundary layer thickness (green). Bottom row: backscatter intensity (normalized units).

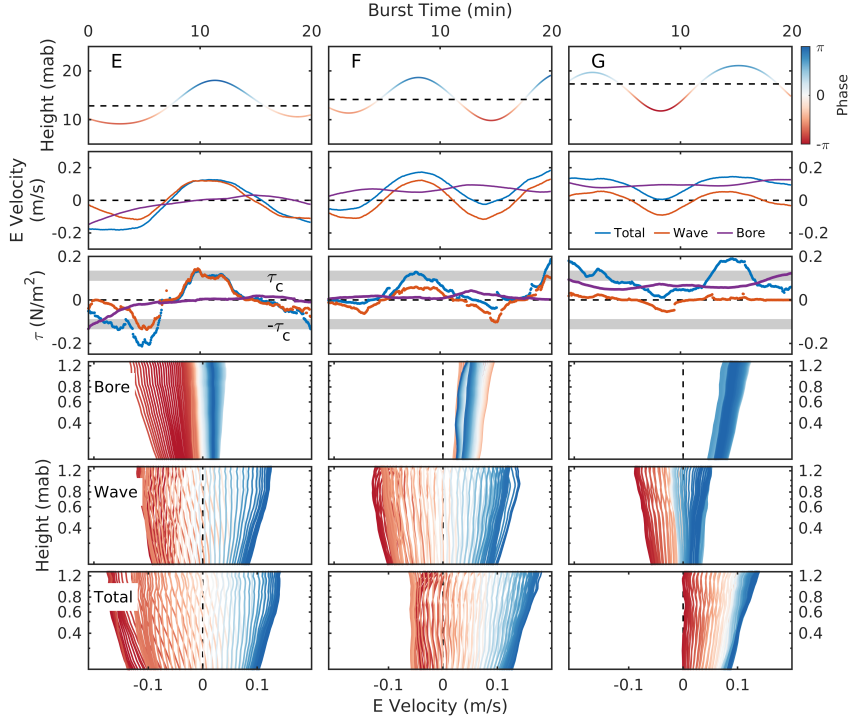


Figure 9. Decomposition of the observations into bore and internal wave components. Rows, from top to bottom: Pycnocline elevation and magnitude of flow velocity; east component of velocity; signed bottom stress (log-layer model) computed independently for the bore and internal wave components, compared with the total stress; vertical structure of east component of the velocity for bore component, wave component and total flow. The velocity time series shown are measured at 1.68 mab (topmost valid measurement bin of the down-looking ADP).

0.2 was consistent with that from empirical flume data for steady flow (e.g., Nielsen, 1992, Figure 3.6.2). Likewise, the time-averaged hydraulic roughness scale obtained from the log velocity fit $z_0 = 1$ cm appears to be consistent with bedform roughness (, ?):

$$z_0 \approx h_{bf}^2 / \lambda_{bf}, \quad (9)$$

and the bottom elevation and length scales, respectively, $h_{bf} = 5$ cm and $\lambda_{bf} = 25$ cm measured by the pencil beam instrument (figure 10). At the back of the bore, the flow velocities are weaker, and less likely to mobilize sediment.

A much weaker bedload transport is expected during the internal waves (bursts *E-H*) when the maximum bottom stress barely exceeds the threshold range for mobilization of d_{50} . The contribution of the internal wave packet riding on the back of the bore is somewhat surprising: the waves are not skewed and symmetric, which would indicate that the velocities are also not skewed; but the acoustic backscatter is strongly correlated with the wave crests, therefore generating eastward (shoreward) transport (figure 4, second row of panels). The reason of this effect becomes clear if the pycnocline and velocity signal are decomposed into the bore and internal wave bands (figure 9). While the pycnocline and velocity oscillation associated with the interval waves are indeed relatively not skewed and symmetric, they are superposed on the larger bore oscillation. While during burst *E* the phase of east component of the bore flow coincides with the phase of the wave flow, during bursts *F* and *G* the bore flow is strictly positive (eastward, shoreward), skewing the total flow eastward, reducing the westward flow phase, and en-

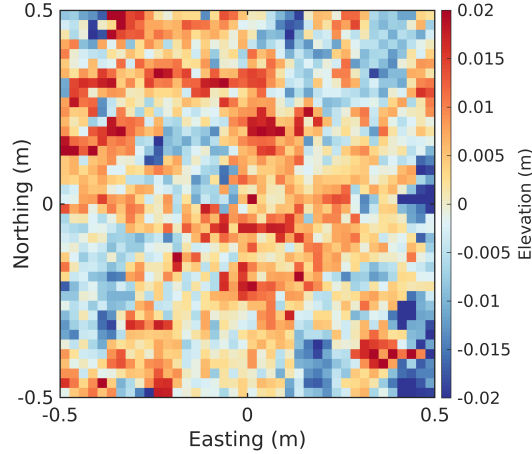


Figure 10. Bed elevation relative to the mean, estimated from pencil beam sonar (Sep 15th, 2017, 05:28 hr).

hancing the eastward one. The friction velocity is also reduced/increased accordingly, with the net result that the bottom stress exceeds the critical value for mobilization only in the eastward direction – the bottom stress approaches or exceeds the mobilization threshold only under the crest, in the positive direction. It is interesting to note that during bursts *E-G* neither the bore nor the waves alone would generate large enough stresses for sediment mobilization.

4 Discussion

The Inner Shelf Dynamics Experiment conducted in September 2017, organized by the Naval Research Laboratory and the Office of Naval Research and involving 14 universities and research institutions (e.g., McSweeney et al., 2019; Kumar et al., 2021) collected a uniquely rich data set that provides an unprecedented opportunity to gain insight into internal waves dynamics on the coast of California, US. The study presented here is limited to a very small part of this huge data set: we analyze the flow structure of a 6-hrs tidal bore observed on Sep. 15, 2017 by the NRL35N instrument cluster deployed by the Navy Research Laboratory near the 35-m isobath. Our goal is to gauge the sediment transport ability of such a large scale wave.

The observations suggest that the bore is undergoing a weakly nonlinear shoaling process that transforms into a dispersive shock (“solibore”) wave: the front of the bore steepens and radiates internal waves with a much shorter scales (≈ 15 -min period). The asymmetry of the tidal bore skews negative (with respect to the propagation direction) the flow velocities, increasing significantly the flow under the bore trough. The large velocities at the bore trough generate bottom stresses large enough to mobilize sediment. In the shoaling case, this means seaward sediment transport. However, the sediment transport problem is complicated by the radiation of smaller scale internal waves. In the case of the Sep. 15th bore, the wave packet is has large amplitudes (in the order of 3 m) and generates flow velocities that match in the bore flow magnitude. The superposition of the two scales of oscillation modulates the weaker positive flow at the bore back, enhancing it enough to generate bottom stresses capable to mobilize sediment. This mechanism generates *shoreward* transport. The question of the direction of the net transport is difficult to settle, however, without direct measurements of mobilized sediment. A schematic of the transport mechanism is shown in figure (11).

As difference between transport by bore and by bore-modulated internal waves (terms of likely same order of magnitude), the net transport direction and magnitude under shoaling tidal bores depends critically on the details of the bore evolution. Assume that the weakly shoaling bore goes through the typical stages of steepening, followed by internal wave radiation. Over the steepening domain, the bore may induce negative sediment transport, increasing in intensity as its asymmetry increases. However, as internal waves are radiated, positive transport under wave packet increases, possibly balancing or exceeding the negative transport. Sediment hysteretic processes, e.g., bed “softening” by the preceding passage of the bore trough, might increase transport by waves. The weight of these effects depends on the initial bore nonlinearity, and the number and rate of internal waves radiated, as well as the bathymetric forcing characteristics (slope, depth), and stratification. This discussion should also be placed in the context of the different types of bore evolution and breaking, aspects that have not been discussed here.

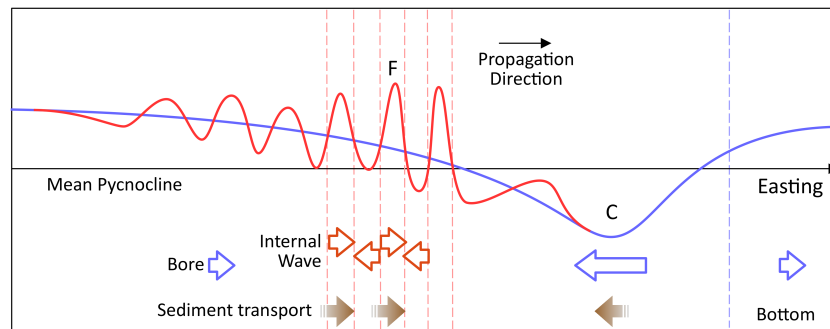


Figure 11. Schematic of sediment transport under a weakly shoaling internal bore, in a spatial representation. The seaward flow (blue arrow) under the bore trough generates seaward transport (brown arrow) that increases in intensity as the bore front steepens. At the back of the bore, the flow associated with radiated internal waves (red arrows) modulates the weak shoreward bore flow (blue arrow), decreasing the bottom stresses under wave troughs and increasing it under crests, generating shoreward sediment transport (brown arrows). The net transport direction and magnitude depends on the initial nonlinearity and the stage in the weak shoaling evolution.

Data Availability Statement

Data stored in a repository managed by the UCSD Library Digital Collections was used in the creation of this manuscript (Kumar et al., 2020). The subset of data was collected during the 2017 Inner Shelf dynamics experiment (Kumar et al., 2021).

Acknowledgments

The author thanks members of the Office of Naval Research (ONR) for the technical support in planning and executing field experiments.

References

- Aghsaee, P., & Boegman, L. (2015). Experimental investigation of sediment resuspension beneath internal solitary waves of depression. *J. Geophys. Res. Ocean.* (May 2015), 775–791. doi: 10.1002/2015JC011107

- Aghsaee, P., Boegman, L., Diamessis, P. J., & Lamb, K. G. (2012). Boundary-layer-separation-driven vortex shedding beneath internal solitary waves of depression. *J. Fluid Mech.*, *690*, 321–344. doi: 10.1017/jfm.2011.432
- Allen, J. R. L. (1982). *Sedimentary Structures: Their Characters and Physical Basis, Volume I*. Elsevier Scientific Publishing Company.
- Boczar-Karakiewicz, B., Bona, J. L., & Pelchat, B. (1991). Interaction of internal waves with the seabed on continental shelves. *Cont. Shelf Res.*, *11*(8), 1181–1197. doi: 10.1016/0278-4343(91)90096-O
- Boegman, L., & Stastna, M. (2019). Sediment resuspension and transport by internal solitary waves. *Annu. Rev. Fluid Mech.*, *51*, 129–154. doi: 10.1146/annurev-fluid-122316-045049
- Bogucki, D. J., Dickey, T. D., & Redekopp, L. G. (1997). Sediment resuspension and Mixing by Resonantly Generated Internal Solitary Waves. *J. Phys. Oceanogr.*, *27*, 1181–1196. doi: [https://doi.org/10.1175/1520-0485\(1997\)027<1181:SRAMBR>2.0.CO;2](https://doi.org/10.1175/1520-0485(1997)027<1181:SRAMBR>2.0.CO;2)
- Bogucki, D. J., & Redekopp, L. G. (1999). A mechanism for sediment resuspension by internal solitary waves. *Geophys. Res. Lett.*, *26*(9), 1317–1320. doi: 10.1029/1999GL900234
- Cacchione, D. A., & Drake, D. E. (1986, sep). Nepheloid layers and internal waves over continental shelves and slopes. *Geo-Marine Lett.*, *6*(3), 147–152. doi: 10.1007/BF02238085
- Carr, M., Davies, P. A., & Shivaram, P. (2008). Experimental evidence of internal solitary wave-induced global instability in shallow water benthic boundary layers. *Phys. Fluids*, *20*(6). doi: 10.1063/1.2931693
- Diamessis, P. J., & Redekopp, L. G. (2006). Numerical investigation of solitary internal wave-induced global instability in shallow water benthic boundary layers. *J. Phys. Oceanogr.*, *36*(5), 784–812. doi: 10.1175/JPO2900.1
- Goring, D. G., & Nikora, V. I. (2002). Despiking Acoustic Doppler Velocimeter Data. *J. Hydraul. Eng.*, *128*(1), 117–126. doi: 10.1061/(asce)0733-9429(2002)128:1(117)
- Grant, W. D., & Madsen, O. S. (1979). Combined wave and current interaction with a rough bottom. *J. Geophys. Res. Ocean.*, *84*(C4), 1797–1808. doi: 10.1029/jc084ic04p01797
- Helrich, K. R., & Melville, W. K. (2006). Long nonlinear internal waves. *Annu. Rev. Fluid Mech.*, *38*, 395–425. doi: 10.1146/annurev.fluid.38.050304.092129
- Karl, H. A., Cacchione, D. A., & Carlson, P. R. (1986). Internal-wave currents as a mechanism to account for large sand waves in Navarinsky Canyon head, Bering Sea. *J. Sediment. Res.*, *56*(5), 706–714. doi: 10.1306/212F8A21-2B24-11D7-8648000102C1865D
- Kumar, N., Lerczak, J. A., Xu, T., Waterhouse, A. F., Thomson, J., Terrill, E. J., ... Ahn, S. (2020). *Observations and Model Simulations from the Inner-Shelf Dynamics Experiment (ISDE)* [Dataset]. University of California San Diego. doi: 10.6075/J0WD3Z3Q
- Kumar, N., Lerczak, J. A., Xu, T., Waterhouse, A. F., Thomson, J., Terrill, E. J., ... Ahn, S. (2021). The Inner-Shelf Dynamics Experiment. *Bull. Am. Meteorol. Soc.*, *102*(5), E1033–E1063. doi: 10.1175/BAMS-D-19-0281.1
- Levine, M. D. (1983). Internal waves in the ocean: A review. *Rev. Geophys.*, *21*(5), 1206–1216.
- Massel, S. R. (2015). *Internal Gravity Waves in the Shallow Seas* (Vol. 19). Springer.
- McSweeney, J. M., Lerczak, J. A., Barth, J. A., Becherer, J., Colosi, J. A., Mackinnon, J. A., ... Waterhouse, A. F. (2019). Observations of shoaling nonlinear internal bores across the Central California inner shelf. *J. Phys. Oceanogr.*, *49*(10), 111–132. doi: 10.1175/JPO-D-19-0125.1
- Meral, R. (2016). A study on the estimating of sediment concentration with tur-

- 419 bidity and acoustic backscatter signal for different sediment sizes. *Hydrol. Res.*,
 420 47(2), 305–311. doi: 10.2166/nh.2015.109
- 421 Miropol'sky, Y. Z. (2001). *Dynamics of internal gravity waves in the ocean* (Vol. 24;
 422 R. Sadourny, Ed.). Springer.
- 423 Nielsen, P. (1992). *Coastal Bottom Boundary Layers and Sediment Transport*. World
 424 Scientific. doi: 10.1142/1269
- 425 Nittrouer, C. A., & Wright, L. D. (1994). Transport of particles across continental
 426 shelves. *Rev. Geophys.*, 32(1), 85–113. doi: 10.1029/93RG02603
- 427 Noble, M. A., & Xu, J. P. (2003). Observations of large-amplitude cross-shore in-
 428 ternal bores near the shelf break, Santa Monica Bay, CA. *Mar. Environ. Res.*,
 429 56(1-2), 127–149. doi: 10.1016/S0141-1136(02)00328-8
- 430 Quaresma, L. S., Vitorino, J., Oliveira, A., & da Silva, J. (2007). Evidence of sed-
 431 iment resuspension by nonlinear internal waves on the western Portuguese
 432 mid-shelf. *Mar. Geol.*, 246(2-4), 123–143. doi: 10.1016/j.margeo.2007.04.019
- 433 Rayson, M. D., Jones, N. L., & Ivey, G. N. (2019). Observations of large-amplitude
 434 mode-2 nonlinear internal waves on the Australian north west shelf. *J. Phys.*
 435 *Oceanogr.*, 49(1), 309–328. doi: 10.1175/JPO-D-18-0097.1
- 436 Ribberink, J. S. (1998). Bed-load transport for steady flows and unsteady oscillatory
 437 flows. *Coast. Eng.*, 34(1-2), 59–82. doi: 10.1016/S0378-3839(98)00013-1
- 438 Richards, C., Bourgault, D., Galbraith, P. S., Hay, A. E., & Kelley, D. E. (2013).
 439 Measurements of shoaling internal waves and turbulence in an estuary. *J.*
 440 *Geophys. Res. Ocean.*, 118(1), 273–286. doi: 10.1029/2012JC008154
- 441 Sahin, C., Safak, I., Sheremet, A., & Mehta, A. J. (2012). Observations on cohe-
 442 sive bed reworking by waves: Atchafalaya Shelf, Louisiana. *J. Geophys. Res.*
 443 *Ocean.*, 117(9), 1–14. doi: 10.1029/2011JC007821
- 444 Sheng, J., & Hay, A. E. (1988). An examination of the spherical scatterer approx-
 445 imation in aqueous suspensions of sand. *J. Acoust. Soc. Am.*, 83(2), 598–610.
 446 doi: 10.1121/1.396153
- 447 Stastna, M., & Lamb, K. G. (2002). Vortex shedding and sediment resus-
 448 pension associated with the interaction of an internal solitary wave and
 449 the bottom boundary layer. *Geophys. Res. Lett.*, 29(11), 7–1–7–3. doi:
 450 10.1029/2001GL014070
- 451 Sutherland, B. R. (2014). *Internal Gravity Waves*. doi: 10.1017/cbo9781107478701
 452 .007
- 453 Thorne, P. D., & Hanes, D. M. (2002). A review of acoustic measurement of small-
 454 scale sediment processes. *Cont. Shelf Res.*, 22(4), 603–632. doi: 10.1016/S0278
 455 -4343(01)00101-7
- 456 Thorne, P. D., Hardcastle, P. J., & Soulsby, R. L. (1993). Analysis of acoustic mea-
 457 surements of suspended sediments. *J. Geophys. Res.*, 98(C1), 899–910. doi: 10
 458 .1029/92JC01855
- 459 Vallis, G. K. (2017). *Atmospheric and Oceanic Fluid Dynamics*. Cambridge Univer-
 460 sity Press.
- 461 van Rijn, L. C. (1984). Sediment Pick-Up Functions. *J. Hydraul. Eng.*, 110(10),
 462 1494–1502. doi: 10.1061/(asce)0733-9429(1984)110:10(1494)
- 463 Welch, P. D. (1967). The Use of Fast Fourier Transform for the Estimation of
 464 Power Spectra: A Method Based on Time Averaging Over Short, Modified Pe-
 465 riodograms [Journal Article]. *IEEE Trans. Audio Electroacoust.*, 15(2), 70–73.
 466 doi: 10.1109/TAU.1967.1161901
- 467 Whalen, C. B., de Lavergne, C., Naveira Garabato, A. C., Klymak, J. M., MacKin-
 468 non, J. A., & Sheen, K. L. (2020, nov). Internal wave-driven mixing: governing
 469 processes and consequences for climate. *Nat. Rev. Earth & Environ.*, 1(11),
 470 606–621. doi: 10.1038/s43017-020-0097-z
- 471 Zhivomirov, H. (2019). On the Development of STFT-analysis and ISTFT-synthesis
 472 Routines and their Practical Implementation. *TEM J.*, 8/1, 56–64. doi: 10
 473 .18421/TEM81-07

474 Zulberti, A., Jones, N. L., & Ivey, G. N. (2020). Observations of Enhanced Sediment
475 Transport by Nonlinear Internal Waves. *Geophys. Res. Lett.*, 47(19), 1–11. doi:
476 10.1029/2020GL088499